

# Exploring the supernova remnant G308.4–1.4

T. Prinz and W. Becker

Max Planck Institute for extraterrestrial Physics, PO Box 1312, Giessenbachstr., 85741 Garching, Germany

Received [date] / Accepted [date]

## ABSTRACT

**Aims.** We present a detailed X-ray and radio wavelength study of G308.4–1.4, a candidate supernova remnant (SNR) in the ROSAT All Sky Survey and the MOST supernova remnant catalogue.

**Methods.** The SNR candidate and its central point sources were studied using observations from the Chandra X-ray Observatory, SWIFT, the Australian Telescope Compact Array (ATCA) at 1.4 and 2.5 GHz and WISE infrared observation at 24  $\mu\text{m}$ .

**Results.** We conclude that G308.4–1.4 is indeed a supernova remnant by means of its morphology matching at X-ray, radio and infrared wavelength, its spectral energy distribution in the X-ray band and its emission characteristics in the radio band. G308.4–1.4 is a shell-type SNR. X-ray, radio and infrared emission is seen only in the eastern part of the remnant due to a strong spatial density variation of the interstellar medium around the remnant. The X-ray emission can best be described by an absorbed non-equilibrium collisional plasma with a hydrogen density of  $n_{\text{H}} = (1.02 \pm 0.04) \text{ cm}^{-3}$ , a plasma temperature of  $6.3^{+1.2}_{-0.7}$  million Kelvin and an underabundance of Iron, Neon and Magnesium, as well as an overabundance in Sulfur with respect to the solar values. A Sedov analysis revealed that the remnant is at a distance of  $\approx 10 \text{ kpc}$  and the progenitor star exploded  $\sim 5000$  to  $7500$  years ago. Two faint X-ray point sources located near to the remnant's geometrical center are detected. Both sources have no counterpart at other wavelengths, leaving them as candidates for the compact remnant of the supernova explosion.

**Key words.** ISM: supernova remnants - ISM: individual objects: G308.4–1.4- Stars: neutron

## 1. Introduction

Supernovae (SNe), the core-collapse of massive stars or the thermonuclear disruption of white dwarfs, are rare events, occurring on average every 50 years in the Galaxy (Keane & Kramer 2008). However, in the past 2000 years, only 7 Galactic SNe have been observed – SN 185 (RCW 86), SN 386 (G11.2–0.3), SN 1006, SN 1181 (3C58), Crab SN, Tycho SN and the Kepler SN. Most Galactic SNs are unobserved owing to visible-band extinction by interstellar dust. Moreover, only  $\approx 274$  SNR have been identified in the radio band (Green 2009, and references therein). Although the Green catalog represents the results of more than 40 years of intensive search with the largest radio telescopes, it is incomplete and strongly biased by selection effects. For a source to be included in a supernova remnant catalog, it must be (1) extended, with a diameter  $\geq 3'$ ; (2) located at low galactic latitude; and (3) have a non-thermal spectrum with a spectral index in the centimeter-band steeper than 0.3 (Helfand et al. 1989).

Most SNRs emit thermal radiation when the SN blast wave expands in the surrounding interstellar medium (ISM), form a shock wave at the shock front which then ionizes the atoms and increases the temperature to  $10^6 - 10^7 \text{ K}$ . Therefore, the successful completion of the ROSAT All-Sky Survey (RASS) in the X-ray regime provided a new and exciting window for both finding SNRs and the compact objects that may reside within them. The seven X-ray detected and radio-quiet Central Compact Objects which were associated with SNRs (see Gotthelf & Halpern 2008, for a review) are a good example for the impact on pulsar and SN science of X-ray observatories. Additionally, X-ray observations of SNRs at moderate spectral resolution can determine remnants properties like shock velocities, post-shock gas densities and temperature as well as swept-up shell mass and overall morphology.

Busser (1998) and Schaudel (2003) have demonstrated the potential power of X-ray surveys for finding new SNR candidates. They analyzed ROSAT all-sky survey data in a systematic search for extended ( $\geq 5'$ ) X-ray sources at low Galactic latitude ( $b \leq \pm 15^\circ$ ) by correlating them with databases like SIMBAD, NED, NVSS, SUMSS, NRAO, ATNF, Parkes and Effelsberg radio survey data. Finally, they correlated the digital sky survey (DSS II) images for bright optical sources close to the candidate's positions. Of their candidate list 14 sources have been identified meanwhile as SNR (Pfeffermann & Aschenbach 1996; Reich et al. 1992; Busser et al. 1996; Asaoka & Aschenbach 1994; Asaoka et al. 1996; Egger et al. 1996; Folgheraiter et al. 1996; Jackson et al. 2008; Robbins et al. 2011; Stupar et al. 2007; Tian et al. 2010). These identifications suggest that many of their SNR candidates are indeed radio-under-luminous, explaining why past radio surveys could not detect or identify them before.

In a further down-selection of promising candidates our list contains now 9 sources which appear to be very promising SNR candidates. One of them is G308.4–1.4, listed as G308.3–1.4 in Schaudel et al. (2002) and Schaudel (2003). Since the RASS had only an average exposure time of  $\sim 400\text{s}$  for sources in the Galactic plane the available ROSAT data do not support a detailed spectral and spatial analysis of these sources. However, G308.4–1.4 appears in the RASS data as a spherical center-filled X-ray source whereas in the Sydney University Molonglo Sky Survey (SUMSS) two radio arcs have been detected which partly overlap with the RASS data (see figure 1). Moreover, G308.4–1.4 is listed in the MOST supernovae remnant catalogue as possible SNR candidate (Whiteoak & Green 1996).

In this paper we report on the identification of the SNR candidate G308.4–1.4 as SNR using archival Chandra, SWIFT, ATCA and WISE observations. The results of the spatial and

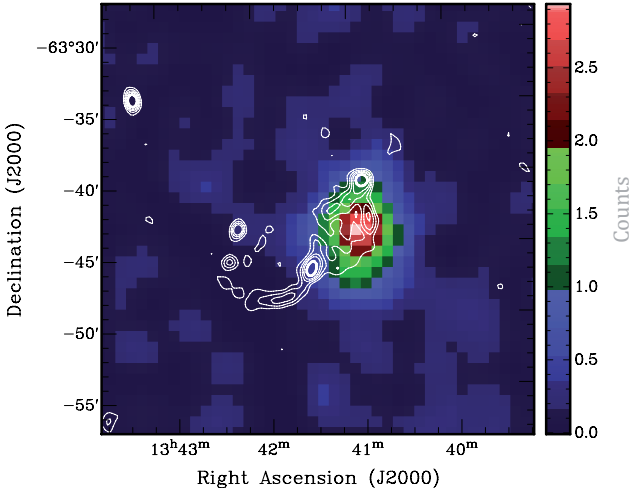


**Fig. 1.** ROSAT RASS  $30' \times 30'$  image of G308.4–1.4 (0.1–2.4 keV) overlaid with the MOST survey image at 843 MHz (contour lines at 4, 8, 12, 16 and 25 mJy). The half-power beamwidth of the telescope is  $43''$ . The RASS image is binned with  $0.75'$  per pixel and smoothed by a Gaussian kernel of  $\sigma \approx 2'$ . The color bar at the right specifies the color assignment in units of counts/image pixel.

spectral analysis of the X-ray and radio data are presented in §2 and §3, respectively. In §4 we report on data of G308.4–1.4 in other wavelength regimes. A summary and a concluding discussion about the identification of G308.4–1.4 and its central point sources is given in §5. Furthermore, in the same section we use the inferred spectral parameters of the SNR to derive fundamental parameters of the remnant.

## 2. X-ray observations and data analysis

The SNR-candidate G308.4–1.4 was observed with the Advanced CCD Imaging Spectrometer (ACIS-I) on board the Chandra X-ray observatory on 26th and 27th of June 2010 (obs.ID. 11249) for  $\approx 15.1$  ks. All data were uncontaminated by soft proton flares. After dead-time correction we were left with 14.9 ks of good data. Standard processed level-2 data were used with the newest de-gap and tap-ringing corrections applied. The reduction of the data was done with the Chandra Interactive Analysis software CIAO, version 4.3. For the spectral fitting we used the XSPEC software package, version 12.7.0.

In addition to Chandra we made use of the SWIFT observatory to analyze X-ray point sources detected in the central region of the remnant. G308.4–1.4 was observed three times with the Swift X-ray Telescope (XRT) on the 17th of June (obs.ID 00032030001), the 7th (obs.ID 00032030002) and the 11th of August (obs.ID 00032030003) for 3.5 ks, 4.2 ks and 1.3 ks, respectively. These data were reduced with the HEASOFT software package, version 6.11. For the spatial and spectral analysis we use the high resolution Chandra data as it contains five times more counts of G308.4–1.4.

To calculate the error in the X-ray flux we used the XSPEC tool `fluxerror.tcl`<sup>1</sup>. For the analysis of the extended source emission we restricted the energy range to 0.5 – 4.0 keV. All errors in this publication represent the  $1\sigma$  confidence range for one parameter of interest, unless stated otherwise.

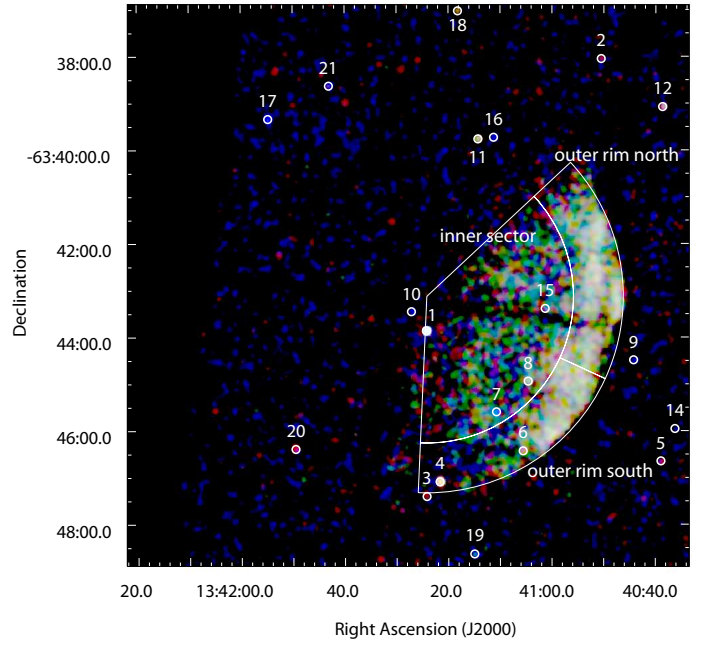


**Fig. 2.** Chandra ACIS-I color image of G308.4–1.4 (red 0.1–1.0 keV, green 1–1.5 keV and blue 1.5–5 keV). The images are binned with  $1''$  per pixel and smoothed by a Gaussian kernel of  $\sigma = 3''$ . 20 point sources are detected in the  $12' \times 12'$  area around the center of G308.4–1.4 (c.f. table 1).

### 2.1. Spatial analysis

Inspecting Fig. 1, the X-ray image of G308.4–1.4 shows strong emission in the eastern part. This region has a circular shape with a diameter of  $\sim 8.4$  arcmin (see fig. 2). The radiation is fading towards the geometrical center of the source. The coordinate of the circle center is  $RA_c \approx 13^h41^m24.9^s$ ,  $DEC_c \approx -63^\circ43'07.8''$  which was obtained by fitting an annulus to the outer skirts of the extended emission.

Searching for point sources in a  $12' \times 12'$  box around G308.4–1.4 using the wavelet source detection algorithm `wavdetect` we found 21 sources. Their position, positional error and signal-to-noise ratio is listed in table 1 and marked by a circle in figure 2. Cross-correlating the sources with the help of the VizieR online tool we found seven matches.<sup>2</sup> These are listed with the positional discrepancy in table 1.

Eight of the detected sources are located within the extended emission of G308.4–1.4 and two of them (# 1 and # 10) are within  $\approx 1$  arcmin of the geometrical center of the SNR-candidate. Source 1 is the brightest among all detected point sources and its designation is CXOU J134124.22–634352.0. However, its position is coincident with 2MASS J13412422–6343520. In the optical source catalogs this source has no information about its proper motion. Hence we cannot put better constraints on the positional coincidence of source # 1 and the 2MASS object. Source 10 has no optical counterpart and is designated with CXOU J134127.12–634327.7.

### 2.2. Spectral analysis of G308.4–1.4

To extract the spectra of the SNR-candidate we first removed all point like sources and then selected all photons in a circular sector with a radius of 4.2 arcmin and central angle of  $\approx 136^\circ$

<sup>1</sup> <http://heasarc.nasa.gov/xanadu/xspec/fluxerror.html>

<sup>2</sup> <http://vizier.u-strasbg.fr/viz-bin/VizieR>

**Table 1.** Detected sources in a  $12' \times 12'$  box around G308.4–1.4. The sources are denoted as in figure 2.

Source	RA (J2000)	DEC (J2000)	$\delta$ RA	$\delta$ DEC	$S/N^a$	optical counterpart (positional discrepancy)
	h:m:s	d:m:s	arcsec	arcsec	$\sigma_G$	
1	13:41:24.217	-63:43:52.04	0.41	0.40	63.0	2MASS J13412422–6343520 (0.07')
2	13:40:50.534	-63:38:03.12	0.45	0.42	2.7	
3	13:41:24.203	-63:47:24.47	0.70	0.42	3.1	
4	13:41:21.634	-63:47:05.63	0.44	0.43	25.5	2MASS J13412162–6347053 (0.27')
5	13:40:38.921	-63:46:38.83	0.54	0.45	3.3	2MASS 13403887–6346384 (0.48')
6	13:41:05.585	-63:46:25.89	0.47	0.42	4.9	
7	13:41:10.742	-63:45:36.11	0.52	0.42	4.9	
8	13:41:04.580	-63:44:56.66	0.52	0.42	6.7	
9	13:40:44.230	-63:44:29.50	0.65	0.41	2.4	
10	13:41:27.121	-63:43:27.72	0.56	0.44	3.8	
11	13:41:14.267	-63:39:45.91	0.57	0.43	9.7	3UC 053–222814 (0.02')
12	13:40:38.666	-63:39:04.77	0.61	0.43	9.0	2MASS J13403862–6339044 (0.41')
13	13:41:02.437	-63:38:00.00	0.56	0.44	0.8	
14	13:40:36.217	-63:45:57.41	0.47	0.44	2.0	
15	13:41:01.308	-63:43:23.50	0.40	0.40	2.9	
16	13:41:11.249	-63:39:44.07	0.76	0.44	4.7	
17	13:41:54.767	-63:39:20.68	0.91	0.67	6.7	2MASS J13415473–6339207 (0.22')
18	13:41:18.147	-63:37:01.87	1.31	0.53	3.8	
19	13:41:14.934	-63:48:38.00	0.67	0.54	3.2	
20	13:41:49.497	-63:46:23.59	1.06	0.65	4.1	
21	13:41:43.058	-63:38:38.10	1.24	0.50	5.4	2MASS J13414304–6338371 (0.93')

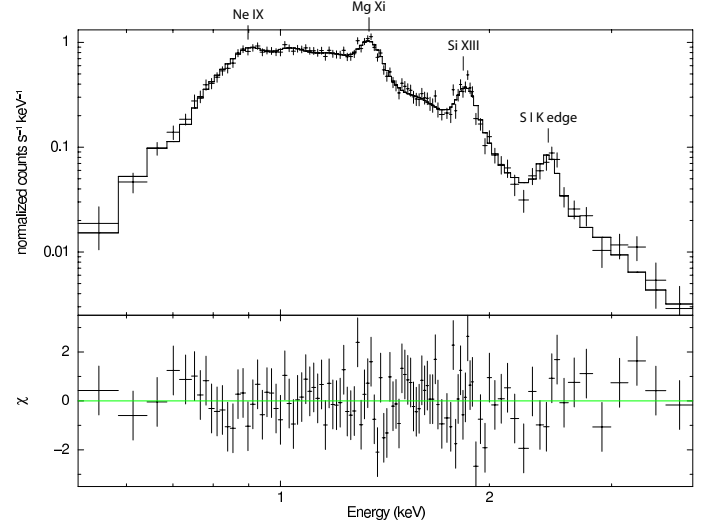
<sup>a</sup>  $\sigma_G = 1 + \sqrt{c_{bg} + 0.75}$ , where  $c_{bg}$  are the background counts.

(see figure 2). The background spectrum was derived from all photons in an annular sector with the same central angle as the circular one but with the radii  $5.5'$  and  $7.2'$ . After subtraction of the background contribution (0.054 cts/pix) we were left with 11 752 counts for the spectral analysis of the whole remnant-candidate. Additionally, the emission region of G308.4–1.4 was divided into three separate regions which are illustrated in figure 2. The net counts are 4095 for the inner sector and 7658 for the outer shell, as well as 4499 for the northern part of the outer shell and 3158 for the southern part. The spectrum of every single region was binned with at least 50 counts per bin. Only the spectra of the southern and northern parts of the outer rim were binned with at least 75 counts per bin.

To fit the X-ray spectrum of G308.4–1.4 we tried various one- and two-component spectral models. However, only a model of an absorbed collisional plasma which is in non-equilibrium and allows a temperature evolution (Borkowski et al. 2001) reproduces the energy distribution of the extended source. In XSPEC this model is implemented as *vgnei*. To improve the goodness of the fit and to obtain the abundance of metals in the plasma we thawed the parameter of every single metal and monitored the improvement of the fit statistic.

The analysis results in a best-fit model with a reduced  $\chi^2$  of 1.03 for 95 degrees of freedom (d.o.f.) and a hydrogen column density  $n_H = 1.02 \pm 0.04 \times 10^{22} \text{ cm}^{-2}$ . The value for  $n_H$  is smaller than the integrated hydrogen column density towards G308.4–1.4 which is  $1.31 \times 10^{22} \text{ cm}^{-2}$  (Kalberla et al. 2005) and  $1.45 \times 10^{22} \text{ cm}^{-2}$  (Dickey & Lockman 1990). The temperature of the plasma is found to be  $6.3^{+1.2}_{-0.7}$  million Kelvin. The best-fit was obtained when thawing the abundance in Neon, Magnesium, Sulfur and Iron which differs significantly from the solar values:  $\text{Ne} = (0.72 \pm 0.14) \text{ Ne}_\odot$ ,  $\text{Mg} = 0.70^{+0.09}_{-0.08} \text{ Mg}_\odot$ ,  $\text{S} = 2.3^{+0.7}_{-0.8} \text{ S}_\odot$  and  $\text{Fe} = 0.70^{+0.14}_{-0.12} \text{ Fe}_\odot$ . The ionization timescale  $\tau_0 = t_0 N_e$  ( $t_0$  is the remnant's age and  $N_e$  the post-shock electron number density) is  $2.7 \times 10^{10} \text{ s/cm}^3$  and the ionization timescale-averaged temperature  $\langle kT \rangle = \int_{t_s}^{\infty} T(t) N_e(t) dt / \tau = 1.2^{+2.2}_{-0.4} \text{ keV}$  ( $t_s$  is the time of the

shock). Thus, the un-absorbed flux in the energy band  $0.5 - 4.0 \text{ keV}$  of G308.4–1.4 is  $f_X = 1.61^{+0.15}_{-0.23} \times 10^{-10} \text{ ergs cm}^{-2} \text{ s}^{-1}$ . The model fit and the raw spectrum is shown in figure 3 and the fitted parameters are listed in table 2.

**Fig. 3.** Spectrum and fitted model of the X-ray emission of the whole remnant.

Adding a second *gnei* component results in  $\chi^2_{red} = 1.06$  for 91 d.o.f. and hence is no improvement over a single model. The other models we have tried to fit to the spectral distribution are a VMEKAL-model ( $\chi^2_{red} = 2.92$  for 96 d.o.f.), a VAPEC-model ( $\chi^2_{red} = 2.34$  for 96 d.o.f.) and a thermal bremsstrahlung model ( $\chi^2_{red} = 7.7$  for 101 d.o.f.). None of these models can reproduce the spectrum of G308.4–1.4. However, all three model fits re-

sults in a  $n_H \approx 1 \times 10^{22} \text{ cm}^{-2}$  and a plasma temperature of  $\sim 0.5$  keV.

### 2.2.1. The inner sector and the outer rim

To investigate the spatial variation of the hot plasma we have divided the extended source into two regions, the inner sector and the outer rim. Additionally, the outer rim was divided into two parts, north and south (see figure 2 for a illustration). For the background spectra of the four regions we used the same area on the detector as for the whole remnant, only for the outer rim north and south we used a center angle that matched the one from the source regions.

First we fitted the plasma model with free  $n_H$ . In every of the four spectral fits we found a hydrogen column density which is in good agreement with the  $n_H$  of the whole remnant. Second we fitted the spectra with a  $n_H$  fixed to the value of the whole remnant. The fitted value for  $n_H$  and the results of the fits with a frozen  $n_H$  are summarized in table 2 and the spectra with the respective fits are shown in figure 4.

Within the statistical uncertainties, all examined regions turn out to have a similar temperature. Only the ionization timescale-averaged temperature is varying. The large statistical uncertainty also prevents us from concluding on a temperature evolution with the distance to the expected center of the remnant. No variation of the Neon and Magnesium abundance over the surface of the remnant is detectable too. The only noticeable change in abundance is in Sulfur and Iron in the outer rim. The spectrum in the northern rim shows an abundance in Iron comparable with the solar value. In the southern rim no significant deviation from the solar value was found in the abundance of Sulfur. The ionization timescale varies with distance from the remnant's center and the direction of the expanding shock wave into the ISM. The highest values for  $\tau$  were found for the inner sector ( $8.1 \times 10^{10} \text{ s/cm}^3$ ) and the lower one in the southern part of the rim ( $2.0 \times 10^{10} \text{ s/cm}^3$ ) which implies a different post-shock electron number density in the inner and outer regions of the SNR-candidate.

### 2.3. The central point sources

As mentioned above, two point sources were detected close to the presumed center of the remnant, source # 1 (CXOU J134124.22–634352.0) and # 10 (CXOU J134127.12–634327.7). For the spectral analysis of source # 1 we used all photons within a circular region of radius 10 arcsec centered on the source position. The background was extracted from an annulus with radii 15'' and 20''. After background correction we were left with 195 source counts in the energy band between 0.5 and 10.0 keV. We used the tool `psextract` to compute the response matrices and binned the spectrum with at least 20 counts per bin.

A single absorbed blackbody or a single absorbed power law model for fitting the spectral distribution gives poor results. In the case of a blackbody spectrum the reduced  $\chi^2 = 2.67$  for 6 degrees of freedom is unacceptably large. The power law model fit results in a reduced  $\chi^2$  of 0.94 (6 d.o.f.). However, the post-fit residuals show systematic derivations between the data points and the fitted model. Therefore, we used a two-component absorbed blackbody model which results in  $\chi^2 = 1.62$  (4 d.o.f.) and a  $n_H = 1.34^{+1.80}_{-1.31} \times 10^{22} \text{ cm}^{-2}$ . In order to better constrain the spectral parameters we fixed  $n_H$  to the hydrogen column density obtained from fits to G308.4–1.4. This gave a reasonable fit with

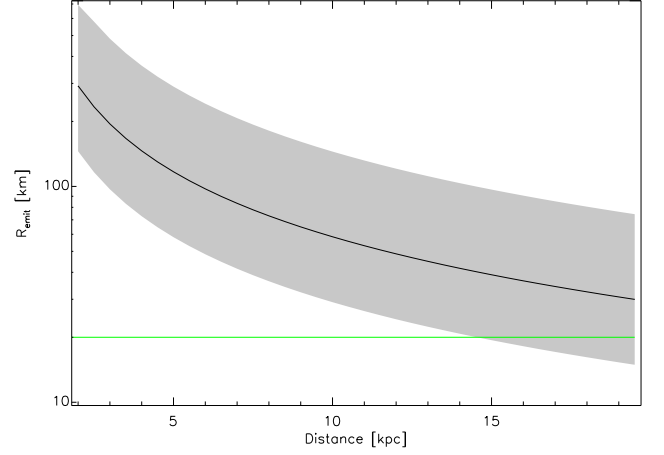


**Fig. 5.** Dependence of the blackbody emitting radius  $R_{\text{emit}}$  on the distance to source # 1 in kpc. The error range is gray shaded and the green line indicates the upper limit on the radius of a neutron star.

$\chi^2 = 1.96$  for 5 d.o.f. (see figure 6). The temperatures of the two blackbodies are  $T_1 = 1.3^{+0.3}_{-0.2} \times 10^6 \text{ K}$  and  $T_2 = 6.4^{+2.8}_{-1.4} \times 10^6 \text{ K}$ . Using the normalization factors  $K_1 = 7^{+21}_{-5} \times 10^{-5}$  and  $K_2 = (1.3 \pm 0.4) \times 10^{-6}$  of the two blackbodies and the distance to the source  $D_{10}$  in units of 10 kpc we estimate the emitting source radius  $R$  as follows:

$$R = \sqrt{\frac{K \times 10^{39}}{4\pi\sigma_B D_{10}^2 T^4}} \text{ [m]}, \quad (1)$$

where  $\sigma_B$  is the Stefan-Boltzmann constant. As we do not know the distance to G308.4–1.4 we consider the emitting radius as function of the distance to the source. This is illustrated in figure 5. The result for the second blackbody is  $R_2 = 340^{+303}_{-158} d_{10}^{-1} \text{ m}$ . The un-absorbed flux in the energy band 0.5 to 10 keV is  $f_X = 2.2^{+0.5}_{-1.9} \times 10^{-12} \text{ ergs cm}^{-2} \text{ s}^{-1}$  and in the energy band 0.3 to 3.5 keV  $f_X = (4 \pm 2) \times 10^{-12} \text{ ergs cm}^{-2} \text{ s}^{-1}$ .

Additionally, we tried a model composed of a blackbody and a power law with the same fixed  $n_H$  as before. This gives a reasonable fit with  $\chi^2 = 2.17$  (5 d.o.f.). The photon index is  $2.4^{+1.0}_{-1.2}$  and the blackbody temperature is  $(1.3 \pm 0.3) \times 10^6 \text{ K}$ . With the normalization of  $K_1 = 9^{+53}_{-7} \times 10^{-5}$  the emitting radius is  $75^{+220}_{-46} d_{9.8}^{-1} \text{ km}$ . The un-absorbed flux in the energy band 0.5 to 10 keV is  $f_X = 2.5^{+0.5}_{-2.3} \times 10^{-12} \text{ ergs cm}^{-2} \text{ s}^{-1}$ .

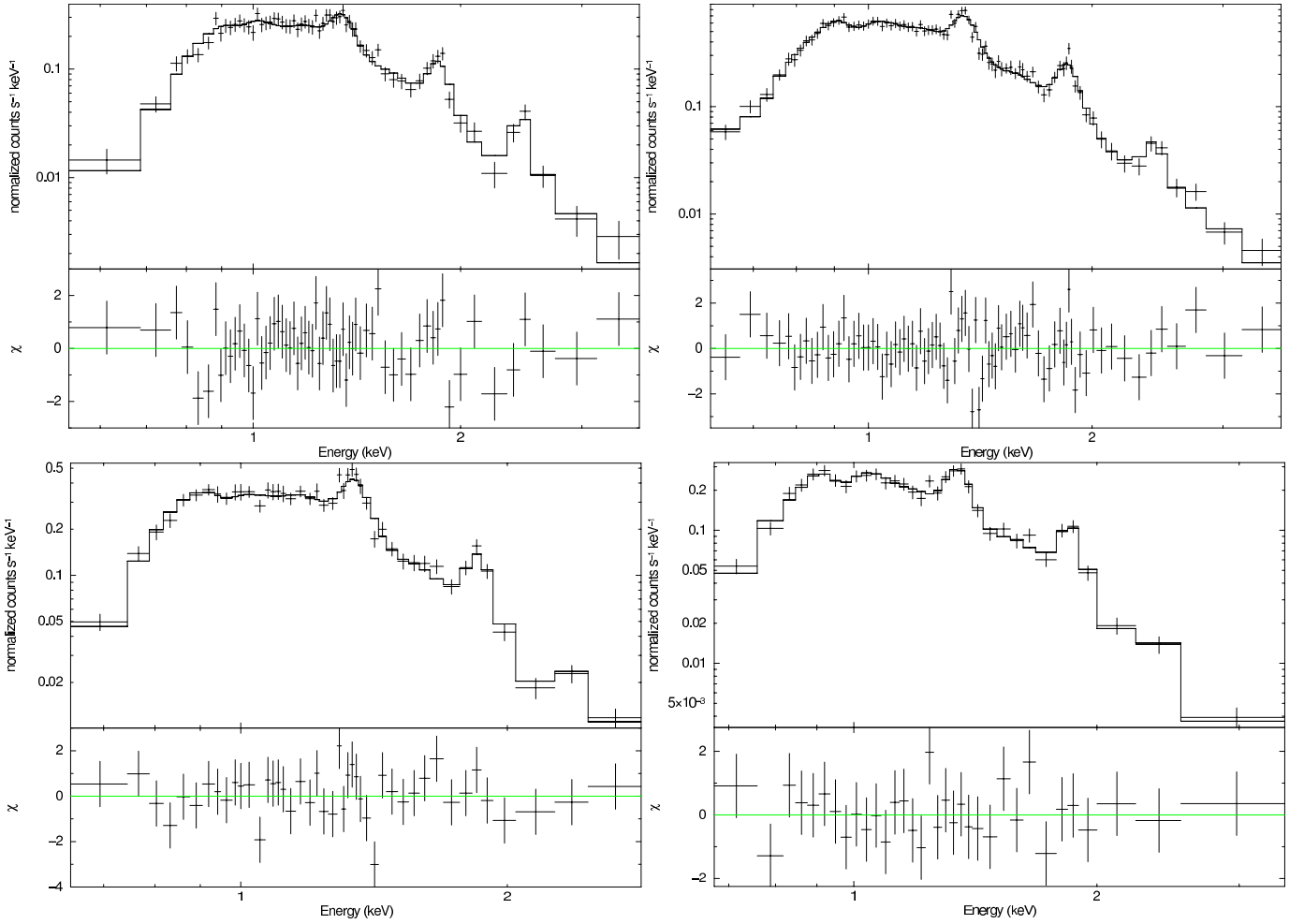
As mentioned in section 2.1 the position of source # 1 is consistent with 2MASS J13412422–6343520, a star with a magnitude of  $B = 19.7$ ,  $R = 19.6$ ,  $J = 14.0$ ,  $H = 13.3$  and  $K = 13.1$ . This implies an X-ray-to-visual flux ratio of  $\log(f_X/f_V) = \log(f_X) + V/2.5 + 5.37 = 1.55$  (Maccacaro et al. 1988). Here  $f_X$  is the X-ray flux in the 0.3–3.5 keV band in  $\text{ergs cm}^{-2} \text{ s}^{-1}$ ,  $V$  is the visual magnitude and we assumed that  $V \approx R$ . For stars the ratio should be in the range  $\log(f_X/f_V) = -2.46 \pm 1.27$  (Krautter et al. 1999).

In addition we tried to fit various plasma models to the source spectrum. The only reasonable fit was found when using a APEC model. The goodness of fit which we found for 6 d.o.f. was  $\chi^2_{\text{red}} = 0.78$  for the following spectral parameters:  $n_H < 0.47 \times 10^{22} \text{ cm}^{-2}$ ,  $T = 3.1^{+1.7}_{-1.4} \times 10^7 \text{ K}$ . For this model the flux in the 0.3 to 3.5 keV range is  $f_X = 1.1^{+0.2}_{-0.1} \times 10^{13} \text{ ergs cm}^{-2} \text{ s}^{-1}$ . Thus, the X-ray-to-visual flux ratio is  $\log(f_X/f_V) = 0.25$ , still

**Table 2.** Detected sources in a  $12' \times 12'$  box around G308.4–1.4. The sources are denoted as in figure 2.

	Whole remnant	Inner rim	Outer rim	Outer rim north	Outer rim south
$n_H$ [ $10^{22} \text{cm}^{-2}$ ]	$1.02 \pm 0.04$	$1.05^{+0.11}_{-0.09}$	$1.00 \pm 0.05$	$1.02 \pm 0.09$	$0.99 \pm 0.9$
$k_B T$ [keV]	$0.54^{+0.10}_{-0.06}$	$0.55^{+0.08}_{-0.10}$	$0.54^{+0.08}_{-0.05}$	$0.50^{+0.12}_{-0.06}$	$0.57 \pm 0.08$
Ne [ $N_{\text{Ne}}$ ]	$0.72 \pm 0.14$	$0.7 \pm 0.3$	$0.73^{+0.15}_{-0.14}$	$0.5 \pm 0.2$	$0.8 \pm 0.2$
Mg [ $N_{\text{Mg}}$ ]	$0.70^{+0.09}_{-0.08}$	$0.80^{+0.20}_{-0.17}$	$0.67^{+0.10}_{-0.09}$	$0.83^{+0.14}_{-0.13}$	$0.62^{+0.14}_{-0.12}$
S [ $N_{\text{S}}$ ]	$2.3^{+0.7}_{-0.8}$	$3.0^{+1.9}_{-1.0}$	$1.7^{+0.8}_{-0.7}$	$2.4^{+1.3}_{-1.0}$	—
Fe [ $N_{\text{Fe}}$ ]	$0.70^{+0.14}_{-0.12}$	$0.90 \pm 0.3$	$0.64^{+0.14}_{-0.12}$	—	$0.45^{+0.19}_{-0.15}$
$\tau$ [ $10^{10} \text{s/cm}^3$ ]	2.7	8.1	2.1	5.2	2.0
$\langle kT \rangle$ [keV]	$1.2^{+2.2}_{-0.4}$	$0.72^{+0.75}_{-0.12}$	$1.4^{+1.6}_{-0.5}$	$0.81^{+0.76}_{-0.15}$	$1.1^{+1.4}_{-0.4}$
Norm [ $10^{-2} \text{cm}^{-5}$ ] <sup>a</sup>	$3.3 \pm 0.9$	$0.9^{+0.5}_{-0.2}$	$2.4 \pm 0.5$	$1.4 \pm 0.4$	$1.0 \pm 0.3$
$\chi^2$	98.19	57.54	76.81	38.74	18.55
d.o.f.	95	57	77	38	27
$f_X$ (0.5–4.0 keV) [ $10^{-10} \text{ergs cm}^{-2} \text{s}^{-1}$ ]	$1.61^{+0.15}_{-0.23}$	$0.30^{+0.01}_{-0.02}$	$1.25^{+0.08}_{-0.09}$	$0.55^{+0.02}_{-0.04}$	$0.56^{+0.07}_{-0.06}$

<sup>a</sup> Norm =  $\frac{10^{-14}}{4\pi[D_A(1+z)]^2} \int N_e N_H dV$ , where  $D_A$  is the angular diameter distance to the source in cm,  $N_e$  and  $N_H$  are the post-shock electron and hydrogen densities in  $\text{cm}^{-3}$ , respectively.

**Fig. 4.** Spectrum and fitted model of the X-ray emission of the various regions. *Upper left:* inner part of the remnant, *upper right:* outer rim, *lower left:* outer rim north and *lower right:* outer rim south.

higher than the normal value for stars. Again no variation in the spectral parameters between the flaring and quiescence epoch

are detectable. All fitted models and their inferred spectral parameters are listed in table 3.



**Table 3.** Spectral fit results of the central point source # 1.

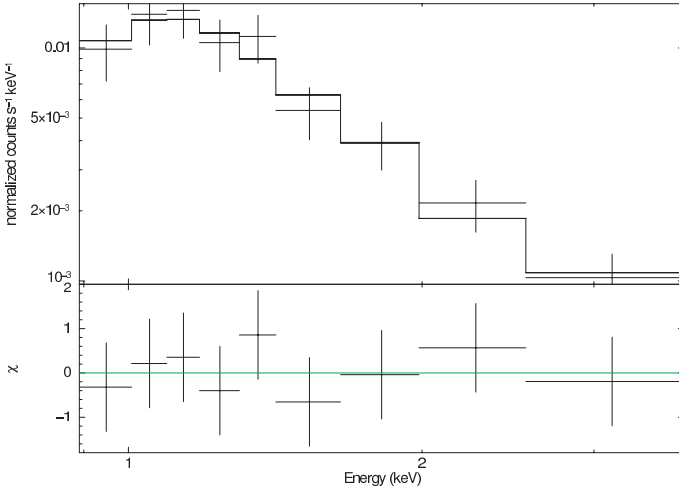
Model	$\chi^2/\text{d.o.f.}$	$n_{\text{H}}$ $10^{22} \text{ cm}^{-2}$	$\Gamma/kT_1$ -/keV	$K_1$	$kT_2$ keV	$K_2$	$f_X^{0.5-10}/f_X^{0.3-3.5}$ $10^{-12} \text{ ergs cm}^{-2} \text{ s}^{-1}$
BB $^{\alpha}, \delta$	16.00/6	$1.2 \times 10^{-4}$	0.44	$9.9 \times 10^{-7}$	—	—	—/—
PL $^{\alpha}, \gamma$	5.62/6	< 0.33	$2.2^{+0.9}_{-0.4}$	$3.9^{+4.3}_{-0.9} \times 10^{-5}$	—	—	$0.16^{+0.03}_{-0.02}/0.16^{+0.04}_{-0.03}$
BB+BB $^{\beta}$	1.96/5	$1.34^{+1.80}_{-1.31}$	$0.11^{+0.03}_{-0.02}$	$7^{+21}_{-5} \times 10^{-5}$	$0.55^{+0.24}_{-0.12}$	$(1.3 \pm 0.4) \times 10^{-6}$	$2.2^{+0.5}_{-1.9}/4 \pm 2$
PL+BB $^{\beta}, \gamma$	2.74/5	< 3.8	$2.4^{+1.0}_{-1.2}$	$7^{+11}_{-5} \times 10^{-5}$	$0.11 \pm 0.03$	$9^{+53}_{-7} \times 10^{-5}$	$2.5^{+0.5}_{-2.3}/5^{+3}_{-4}$
APEC	4.66/6	< 0.47	$2.7^{+1.5}_{-1.2}$	$9.0^{+3.0}_{-1.5} \times 10^{-5}$	—	—	$0.13^{+0.03}_{-0.02}/0.11^{+0.04}_{-0.03}$
BREMS $^{\alpha, \delta}$	6.98/6	$1.8 \times 10^{-9}$	$2.1^{+2.1}_{-0.8}$	$5.1^{+2.3}_{-1.3} \times 10^{-5}$	—	—	—/—
RAYMOND $^{\alpha}$	5.70/6	< 0.21	$2.8^{+2.0}_{-1.1}$	$8.9^{+1.8}_{-0.8} \times 10^{-5}$	—	—	$0.13 \pm 0.02/0.11^{+0.02}_{-0.01}$

$^{\alpha}$  fit shows systematic derivations between the data points and the fitted model.

$^{\beta}$  the spectral parameters are calculated with  $n_{\text{H}}$  fixed to the value obtained in fits to G308.4–1.4.

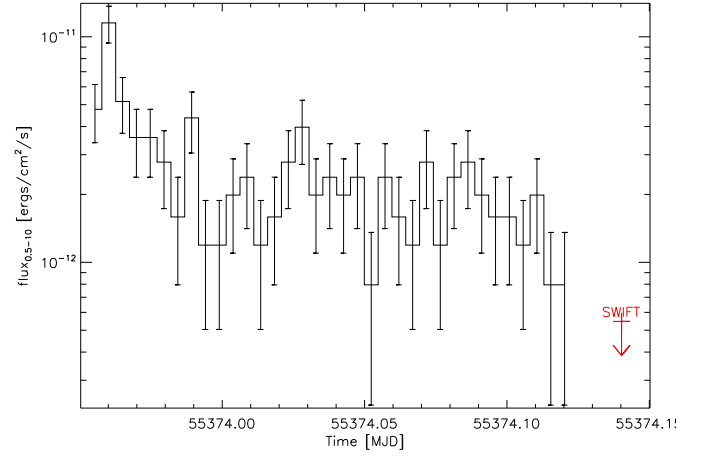
$^{\gamma}$  Power law norm in photons  $\text{keV}^{-1} \text{cm}^{-2} \text{s}^{-1}$  at 1 keV.

$^{\delta}$  some errors could not be calculated.

**Fig. 6.** Spectrum of source # 1 fitted with a double blackbody spectrum.

### 2.3.1. Temporal analysis of source # 1

In order to search for any temporal variability we binned the photon time of arrivals with 400 s per bin (see figure 7). The data show clearly a flare in the first ks of the observation. The spectral parameter of the double blackbody in the flaring and quiescence epoch match the overall spectrum within the error bars. Varying only the normalizations of the two blackbodies the flux in the quiescence epoch is with  $f_X^{0.5-10} = (1.9 \pm 0.3) \times 10^{-12} \text{ ergs cm}^{-2} \text{ s}^{-1}$  slightly lower than the flux in the total exposure. However, the flux in the time interval when the source was flaring is  $f_X^{0.5-10} = (5.2 \pm 1.5) \times 10^{-12} \text{ ergs cm}^{-2} \text{ s}^{-1}$ , three times the quiescence flux. However, the sparse photon statistics lead to large uncertainties in the derived errors of the quiescence and flaring fluxes and thus they are only rough estimates. Merging the SWIFT observations we cannot detect a source at the position of source # 1. In the merged image a total of 4 counts were recorded within a circle with radius 15 arcsec (equals an encircled energy of 70 %) centered on the position of source # 1. The total exposure time of the source was 8344 s. Hence, the  $3\sigma$  upper limit for the counting rate is approximately  $8.6 \times 10^{-4} \text{ cts/s}$ . Using WebPIMMS with the SWIFT response and the spectral

**Fig. 7.** Flux variation of source # 1 in the Chandra observation binned with 400 s per bin and scaled with the mean flux in the whole exposure. The red arrow indicates the  $3\sigma$  upper limit derived with the SWIFT observations.

parameters derived for a double blackbody spectrum the upper limit on the flux is  $\approx 5.3 \times 10^{-13} \text{ ergs cm}^{-2} \text{ s}^{-1}$ . For the APEC model the upper limit is  $\approx 2.3 \times 10^{-14} \text{ ergs cm}^{-2} \text{ s}^{-1}$ . These limits are less than 25 % of the average flux in the Chandra observation, clearly indicating that the source flux is variable on time scales of at least hours to weeks.

### 2.3.2. Extent of source # 1

With the help of a one-dimensional distribution of the counts/0.5'' along a vertical line in the Chandra image around source # 1 we checked if the source is extended. The resulting diagram was obtained by integrating all counts within  $5'' \times 0.5''$  rectangular apertures moving along the western direction with 0.5'' steps. We compared this with the count distribution of a point source simulated with MARX and the spectral information above.<sup>3</sup> However, no excess emission of point source # 1 could be detected.

<sup>3</sup> See <http://space.mit.edu/cxc/marx/>

For source # 10, the other source located close to the center of the remnant, we detected only 8 net counts. Hence, the count rate is  $(5.1 \pm 1.9) \times 10^{-4}$  cts/s, but no spectral analysis is possible by the limited statistics.

### 3. Radio observation and data analysis

The source G308.4–1.4 was observed for 11.25 hours with the Australia Telescope Compact Array, a synthesis telescope near Narrabri, New South Wales on 11th January 2002 at 1.432 and 2.448 GHz with 13 channels per band. The single pointing continuum observations of the source G308.4–1.4 was carried out with the array configuration 0.75C (maximal baseline length is 750 m). All the four Stokes parameters have been recorded.

The flux density calibration was performed through observations of PKS B1934–638, which is the standard primary calibrator for ATCA observations. Phases were calibrated using observations of secondary calibrating sources PKS 1329–665. Since the primary beam response is frequency dependent we did not merge the data from two observing bands before imaging and cleaning. Every single observing run and each of the two observing bands were calibrated separately following the standard procedures for ATCA observations.

The reduction was carried out using the ATNF release of the Multichannel Image Reconstruction, Image Analysis and Display (MIRIAD, Sault et al. 1995). A number of steps in the reduction process (i.e. “flagging”) were done interactively.

Because of the bad phase stability during the observation, the scalar averaging of gains over the interval of 5 min (the length of secondary calibrator’s scan) was performed. Then, a total-intensity continuum image square region was formed using multi-frequency synthesis, uniform weighting and a cell size of 10 arcsec. At the stage of the dirty map production all the correlations with 6th baseline were excluded to obtain an image with better signal-to-noise ratio. The image was then de-convolved using the standard CLEAN algorithm (Clark 1980) with 100 000 iterations and restored. The resulting image was then corrected for the mean primary beam response of the ATCA antennas. Also the separate total-intensity images in both frequency bands were formed. These images were de-convolved using also the CLEAN algorithm (Clark 1980) with 100 000 iterations and then restored and primary beam corrected as the image formed using the data in both frequencies before.

The radio morphology in both frequency bands shows two radio arcs (see figure 8). There are also two radio bright knots within the arcs which do neither have a counterpart in X-rays (see figure 9) nor in the optical (dss2red).

The flux densities of the sources were obtained by integrating the emission within multiple polygons enclosing the remnant. The rms noise in the image measured by similarly integrating over nearby source-free regions. The spectral indices were computed using the total flux density measurements in both available frequencies 1.384 GHz and 2.368 GHz. Fitting the data with a power law  $S \propto \nu^\alpha$ , we obtained a spectral index for the northern knot  $\alpha = -0.05 \pm 0.34$  and for the southern  $\alpha = -0.12 \pm 0.34$ , respectively. The radio emission of the two arcs, however, have a spectral index  $\alpha = -0.71 \pm 0.34$ . (De Horta et al. 2012)

### 4. Observations in other wavelength regimes

The region around G308.4–1.4 was observed in the four infrared bands 3, 5, 12 and 22  $\mu\text{m}$  during the Wide-field Infrared Survey

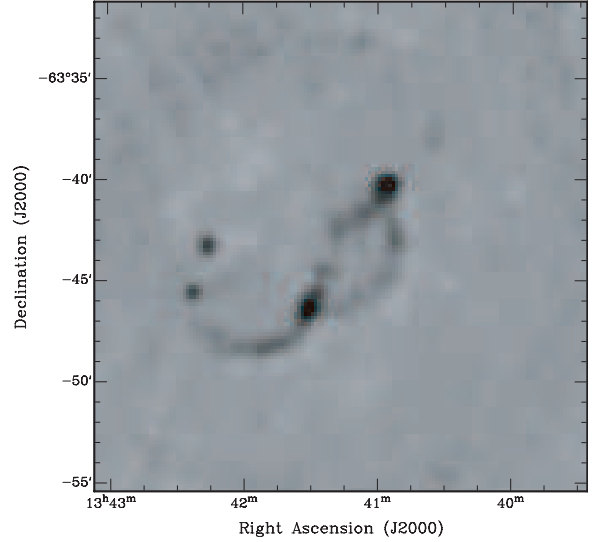


**Fig. 8.** Grey-scale image of the SNR candidate G308.4–1.4 at 1.3 GHz. The gray-scale range is -2 to 24 mJy beam<sup>-1</sup>.

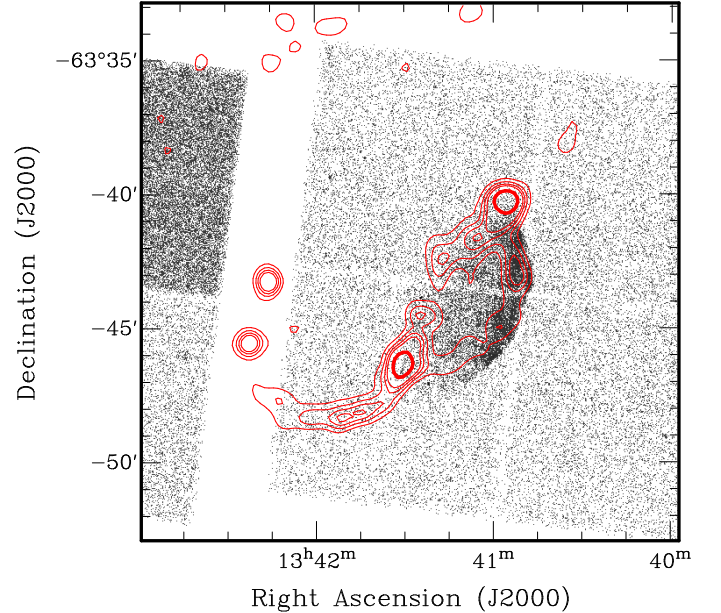


**Fig. 9.** Chandra 20'  $\times$  20' image of G308.4–1.4 overlaid with the ATCA data at 1.4 GHz. The contour levels are 2, 3, 4, 6, 8, 15 mJy beam<sup>-1</sup>. The radio image has a FWHM of  $\sim 43''$  and the X-ray image is binned with 1'' per pixel.

(WISE, Wright et al. 2010). With the 22  $\mu\text{m}$  filter an extended infrared emission, overlapping with the radio and X-ray emission regions, is detectable (see figure 10).

The shock wave of a SN which is running into the interstellar medium can interact with adjacent molecular clouds and produce  $\gamma$ -rays via decays of  $\pi^0$  (Abdo et al. 2011). We therefore checked the archive of the Fermi Large-Area Telescope for a  $\gamma$ -ray source at the position of G308.4–1.4. The Fermi  $\gamma$ -ray satellite monitors the sky continuously since August 2008. However, no source has been detected close to G308.4–1.4 in the Fermi-LAT Second Source Catalog (The Fermi-LAT Collaboration 2011) and inves-

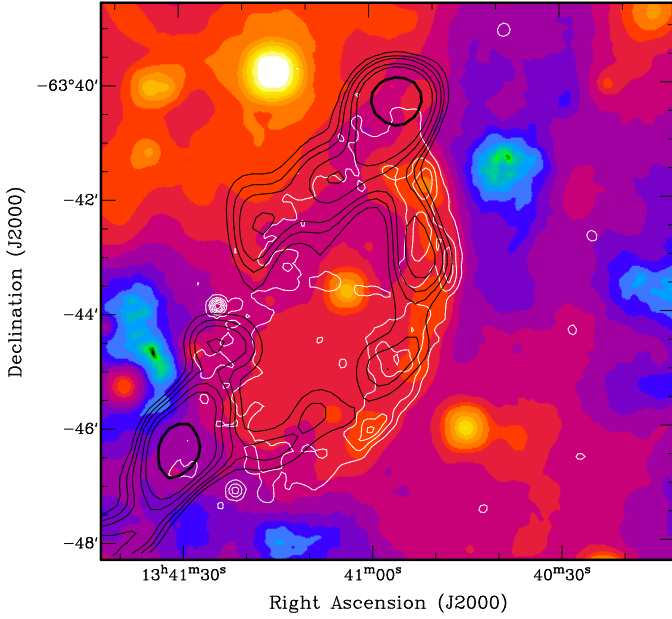


**Fig. 10.**  $10' \times 10'$  WISE image around G308.4–1.4 at 22 micron with the radio contour lines in black at 2, 3, 4, 6, 8 and 15 mJy and the X-ray contours in white.

tingating the images ourselves we found no  $\gamma$ -ray emission matching the X-ray morphology.

## 5. Summary and Discussion

The high resolution imaging and spectroscopic capability of Chandra revealed the X-ray emission of G308.4–1.4 as an extended plasma. The emission region is spherically symmetric with a diameter of 8.4 arc-minutes and an excess emission towards the east.

Comparing the fitted  $n_H$  with the integrated hydrogen column density towards the source of Kalberla et al. (2005) and Dickey & Lockman (1990) places G308.4–1.4 within our Galaxy.

The plasma model which is used to fit the energy distribution of G308.4–1.4 was especially designed to improve the modeling of X-ray spectra of SNR. Other plasma models assume ionization equilibrium and are therefore not able to reproduce the spectra of young SNRs which are not old enough to reach ionization equilibrium (Borkowski et al. 2001). Furthermore, the temperature of the plasma of approximately 6 million Kelvin is in the typical range for SNRs (McKee 1987).

The analysis of the archival ATCA radio data revealed non-thermal emission with a spectral index of  $\approx -0.7$ , which is typical for young to middle-aged SNRs (Dickel 1991). The radio morphology at 0.843, 1.432 and 2.448 GHz is characterized by two arcs. The eastern arc matches well with the X-ray and infrared contours. The second arc which is bending in the west and decreasing brightness towards the center of G308.4–1.4 has no counterpart in other wavelengths. Its origin will be discussed in more detail in section 5.3.

Infrared radiation from SNRs is expected to come either from thermal emission of dust grains in the hot plasma which are heated through collision or from the forbidden lines of elements like Neon, Oxygen and Iron (Seok et al. 2008). Thus, the infrared emission matching the radio and X-ray morphology is another hint that G308.4–1.4 is indeed a SNR.

The lack of  $\gamma$ -ray emission from G308.4–1.4 can be explained by the poor spatial resolution of the Fermi-LAT telescope ( $\sim 1^\circ$  at 1 GeV), which makes it hard to distinguish faint extended sources from the diffuse emission of the Galactic plane. Hence, from the 274 known SNRs only 7 have been detected by Fermi-LAT so far (The Fermi-LAT Collaboration 2011).

There are various physical scenarios to cause a plasma to emit X-rays. However, the two spectral models, APEC and MEKAL, which are normally used to describe the X-ray emission of Galaxy Clusters (ClGs) cannot reproduce the spectrum of G308.4–1.4. Moreover, the temperature of ClGs is normally several  $10^7$  K (Böhringer & Werner 2010), one order of magnitude higher than the fitted value. Thus, we can conclude that G308.4–1.4 is not a ClG. In addition, the possibility of G308.4–1.4 being a planetary nebula (PN) can be ruled out as the X-ray flux of G308.4–1.4 is three orders of magnitude higher than the flux of the brightest PN detected in X-rays, which is at a distance of  $\approx 1$  kpc (Guerrero et al. 2006). Furthermore, the temperature of G308.4–1.4 is a factor of two higher than maximal temperature of the hotter, type 2 PNe (Guerrero et al. 2000).

Based on this results we conclude that G308.4–1.4 is indeed a supernova remnant with its shock wave expanding in more dense ISM in the east. Using the inferred spectral parameters we can estimate fundamental characteristics of the remnant, such as the distance from earth and its age.

### 5.1. Distance

To derive a rough estimate of the distance between SNR G308.4–1.4 and Earth we use a method described by various authors (Sun et al. 1999; Safi-Harb et al. 2001; Gonzalez & Safi-Harb 2003): From the distribution of mean color excess  $\langle E_{B-V} \rangle$  per kiloparsec derived by Lucke (1978) we found  $\langle E_{B-V} \rangle = (0.3 \pm 0.1) \text{ mag kpc}^{-1}$ . Using the fitted hydrogen column density for the whole remnant  $n_H = (1.02 \pm 0.04) \times 10^{22} \text{ cm}^{-2}$ , the relation between the hydrogen column density  $n_H$  and the visual extinction  $A_V$  of Predehl & Schmitt (1995)  $n_H = (1.79 \pm 0.03) \times 10^{21} \text{ cm}^{-2} A_V$  and adopting the relation between  $A_V$  and the color excess  $\langle E_{B-V} \rangle = (3.2 \pm 0.2) A_V$  (Zombeck 2007) the distance to G308.4–1.4 is  $d = 5.9 \pm 2.0$  kpc. We note, that this distance is probably an underestimation of the real distance to G308.4–1.4. This is due to the fact that the mean color excess  $\langle E_{B-V} \rangle$  which we used was derived for reddening layer up to 2 kpc. In the case of distance estimates for Galactic PNe the reddening inferred distances are mostly significantly smaller than distances derived with other methods (Phillips 2006). Thus,  $d \approx 6$  kpc is a lower limit for the distance of SNR G308.4–1.4.

Another approach to determine the distance to G308.4–1.4 uses the fact that the radius of the remnant  $R_s$  can be determined in two ways, where  $R_s$  depend on  $d$  with different exponents. The first equation is a result of the Sedov analysis discussed in the next chapter (equation 4) and depends on  $d^{1/6}$ . The second equation to determine  $d$  is simply the comparison of radius of the remnant in pc ( $R_s$ ) and in arcmin ( $\theta$ ),  $d = R_s/\theta$ , which depends linearly on the distance unit  $d$ . Using this dependencies we derive

$$d = 7420 \cdot (\theta [\text{arcmin}])^{-3/5} \left( \frac{E_{51}}{T_s [\text{K}]} \right)^{2/5} \left( \frac{f}{\text{Norm}} \right)^{1/5} = 9.8^{+0.9}_{-0.7} \text{ kpc}, \quad (2)$$

where  $T_s$  is the post-shock temperature and  $E_{51}$  the SN explosion released kinetic energy in units of  $10^{51}$  ergs. In the following all important quantities are given in units of  $d_{9.8} = d/9.8$  kpc. Using



the flux values deduced for G308.4–1.4 we compute its X-ray luminosity to be  $L_X^{0.5-4} = 1.8^{+0.3}_{-0.2} \times 10^{36} d_{9.8}^{-2} \text{ erg/s}$ .

### 5.2. Age of remnant

First we have to deduce the post-shock hydrogen density  $N_H$ . Using the normalization constant derived in the *vgnei*-model fit and assuming that the hydrogen and electron densities are constant over the volume  $V$  of the emission region we derive the following relation:  $N_e N_H = \text{Norm} \cdot \frac{\pi D_A^2}{10^{-14} V} \text{ cm}^{-6}$ .  $V$  can be approximated by a sphere with radius  $r \approx \frac{4.2\pi}{180} \cdot D$  of which only a fraction of  $\sim \frac{136}{360}$  is bright enough to be detected in the X-ray regime. Therefore,  $V = 1.14 \times 10^{54} (r[\text{arcmin}])^3 d_{kpc}^3 \text{ cm}^3 = 7.98 \times 10^{58} d_{9.8}^3 \text{ cm}^3$ . Here  $d_{kpc}$  is the distance to G308.4–1.4 in kpc. For a fully ionized plasma with cosmic abundances ( $\approx 10\%$  He) the ratio between hydrogen and electron density can be estimated by  $N_H/N_e \approx 0.8$ . Thus, the post-shock hydrogen density  $N_H = (0.77 \pm 0.11) d_{9.8}^{-1/2} \text{ cm}^{-3}$  and the corresponding swept-up mass  $M = 1.4 N_H m_H V \sim 71.7 d_{9.8}^{5/2} M_\odot$  (Slane et al. 2002).

The best fit to the energy spectrum suggest that G308.4–1.4 is in the Sedov-phase. Additionally, the age for the transition from the Sedov-phase into the radiative phase is about 29 kys (Blondin et al. 1998). Therefore, the age of the remnant can be approximated by (McKee 1987)

$$t = 2.71 \times 10^9 \left( \frac{E_{51}}{N_H} \right)^{\frac{1}{3}} T_s^{-\frac{6}{5}} d_{9.8}^{\frac{1}{5}} \text{ yrs.} \quad (3)$$

Assuming that the explosion energy is equal to the canonical value of  $10^{51}$  ergs and the fitted temperature is approximately  $T_s$ , the derived value for the hydrogen density suggest that SNR G308.4–1.4 is  $\approx 5000 - 7500$  years old. Using this result we can calculate the theoretical radius of the remnant (Culhane 1977)

$$R_s = 0.34 \left( \frac{E_{51}}{N_H} \right)^{\frac{1}{5}} t^{\frac{2}{5}} \text{ pc} = 11.9^{+1.9}_{-1.8} d_{9.8}^{\frac{1}{5}} \text{ pc} \quad (4)$$

and the shock velocity (Sedov 1959)

$$v_s = \frac{2 R_s}{5 t} = 730^{+190}_{-160} \text{ km/s,} \quad (5)$$

which is independent on the assumed distance.

The Sedov analysis lead to the conclusion that the SNR is relatively young and is expanding with a velocity in the order of  $\approx 730$  km/s. All fundamental parameters of the SNR are summarized in table 4. However, the numbers in this table should only be seen as rough estimates as we could not determine whether a full temperature equilibrium is already established. If not, a generally higher ion temperature which determines the SNR dynamics, would lead to a higher shock velocity and thus to an e.g. overestimation of the remnant's age.

### 5.3. The central point sources CXOU J134124.22–634352.0 and CXOU J134127.12–634327.7

The X-ray point source CXOU J134124.22–634352.0, located close to the geometrical center of the SNR G308.4–1.4, is seen to exhibit variable and flaring X-ray emission. It lacks a radio counterpart, has no compact/extended X-ray emission as seen in young and powerful pulsars and its best-fit spectral model consists of two blackbodies. Thus, source # 1 shows some properties which have been seen in central compact objects (CCO, see

**Table 4.** Fundamental parameters of SNR G308.4–1.4.

SNR	
distance	$9.8^{+0.9}_{-0.7} \text{ kpc}$
age	$5000 - 7500 \text{ yrs}$
radius	$\sim 4.2'' / 11.9^{+1.9}_{-1.8} d_{9.8}^{1/6} \text{ pc}$
expansion velocity	$730^{+190}_{-160} \text{ km/s}$

Gotthelf & Halpern 2008, for a review). Moreover, one of these CCOs shows flares, 1E 161348–5055 in RCW 103, where its flux changes between  $0.8$  and  $60 \times 10^{-12} \text{ ergs cm}^{-2} \text{ s}^{-1}$ . This is comparable to source #1 where the maximal flux is  $\approx 10^{-11} \text{ ergs cm}^{-2} \text{ s}^{-1}$  and the upper limit derived from the SWIFT observations is  $\approx 5 \times 10^{-13} \text{ ergs cm}^{-2} \text{ s}^{-1}$ .

Using the distance derived in chapter 5.1 the luminosity of CXOU J134124.22–634352.0 is  $L_X^{0.5-10} = 2.5^{+1.2}_{-0.6} \times 10^{34} d_{9.8}^{-2} \text{ erg/s}$ . This is slightly higher than the normal population of CCO (Becker 2009, p.121), only the flaring CCO in RCW 103 has a comparable luminosity of  $0.1 - 8 \times 10^{34} \text{ erg/s}$  (de Luca 2008).

Additionally, the X-ray-to-optical flux ratio and the fitted  $n_H$ , which is in the order of what has been observed for G308.4–1.4, suggest a CCO interpretation for source # 1.

Assuming that the source is indeed the compact remnant of SNR G308.4–1.4 and using the inferred center and the age of the SNR we can derive the proper motion of the object  $\mu = \sqrt{(RA_c - RA_{\#1})^2 + (DEC_c - DEC_{\#1})^2} / t \approx 45.4''/t$ . Using as minimal age the derived lower limit for  $t$  we deduce an upper limit for the proper motion of  $\mu < 17 \text{ mas/yr} \approx 470 \text{ km/s}$ . This limit is higher than the mean two-dimensional proper motion of pulsars in SNRs of  $\sim 227 \text{ km/s}$  (Hobbs et al. 2005), but would not be an exception. For example PSR B1830–08 in SNR W41 has a 2d proper motion of  $\approx 730 \text{ km/s}$ .

Nevertheless, the lower limit of the inferred emitting radius of the blackbody in the BB+BB and PL+BB spectral fit is in the order of the expected value for a neutron star of  $10$  to  $20 \text{ km}$  only if the source is at a distance larger than  $14.5 \text{ kpc}$  (see figure 7). Moreover, we found an infrared and optical source which position is consistent with source # 1. The spectral distribution of the source allows us to fit an APEC model, which Osten et al. (2005) used to model the energy distribution in the X-ray band of the M dwarf flare star EV Lacertae. In addition, the fitted hydrogen column density is consistent to that of a nearby star.

Using the stellar density in direction of G308.4–1.4 we can derive the chance association of the observed 2MASS source with the compact remnant candidate. The chance association is given by  $P_{\text{coin}} = \frac{N}{l_{RA} l_{Dec}} \pi \delta RA \delta DEC$ , where  $N$  is the number of sources detected within a rectangular region of length  $l_{RA}$  and width  $l_{Dec}$ . and  $\delta RA$ ,  $\delta DEC$  are the errors in the position of the source. The 2MASS catalog contains 2206 point-like sources in a box with side length of  $5 \text{ arcmin}$  around the center of the remnant and the chance association is  $1.3\%$ . Thus, the possibility of a false association between the X-ray and the 2MASS source cannot be excluded.

Until now, we did not discuss the western radio arc which has no counterpart in the X-ray and infrared image. The arc could be interpreted as a relativistic radio jet of a source at the geometrical center of the SNR. If so, the central source is either a black hole of stellar mass or a neutron star in a binary system (Mirabel & Rodríguez 1999, and reference therein). Especially the possibility that the central source is a black hole is an inter-

esting speculation which, if proven, would mean that G308.4–1.4 is the remnant of a Type II core-collapse SN, and the first one known which left over a black hole.

To obtain a rough estimate of the source flux of the other source in the center of the remnant, source # 10, we assumed that the source is a CCO, should have at least a spectrum with a blackbody of temperature 2.6 million Kelvin like the CCO in Puppis-A (cf. table 6.4, Becker 2009). Using the WebPIMMS<sup>4</sup> tool with the source count rate and the fitted  $n_H$  of the SNR the flux in the 0.3 – 3.5 keV range is  $f_X \approx 2.2 \times 10^{-14}$  ergs cm<sup>-2</sup>s<sup>-1</sup> and in the 0.5 – 10 keV range is  $f_X \approx 1.9 \times 10^{-14}$  ergs cm<sup>-2</sup>s<sup>-1</sup>. The normalization of a blackbody with this flux, temperature and  $n_H$  is  $2.5 \times 10^{-5}$  which corresponds to an emitting radius of the source of  $\approx 9d_{9.8}^{-1}$  km. This value is in perfect agreement with the expected value for the neutron star radius. The corresponding luminosity in the energy band 0.5 – 10 keV is  $L_X^{0.5-10} = 2.1 \times 10^{32} d_{9.8}^{-2}$  erg/s, a typical value for CCOs. Furthermore, the X-ray-to-visual flux ratio is  $\log(f_X/f_V) > 0.11$  taking into account that no optical source was detected in the USNO-B1.0 catalog and the limiting magnitude of this catalog is 21 (Monet et al. 2003). Thus, no clear evidence for the origin of the emission of source # 10 could be found.

Finally we mention that the detector support structure of Chandra covers the central part of G308.4–1.4 (see figure 2). It is therefore not excluded from our observations that other faint X-ray point sources are located at this position. However, the non-detection of a source in the SWIFT data at the assumed position of the remnant's expansions center sets a strict limit on the flux of such an object.

*Acknowledgements* T.P. acknowledges support from and participation in the International Max-Planck Research School on Astrophysics at the Ludwig-Maximilians University. The authors acknowledge discussions with M. D. Filipović and would like to thank him for his helpful inputs.

## References

- Abdo, A. A., Ackermann, M., Ajello, M., et al. 2011, *ApJ*, 734, 28
- Asaoka, I. & Aschenbach, B. 1994, *A&A*, 284, 573
- Asaoka, I., Egger, R., & Aschenbach, B. 1996, in *Roentgenstrahlung from the Universe*, ed. H. U. Zimmermann, J. Trümper, & H. Yorke, 233–234
- Becker, W. 2009, in *Astrophysics and Space Science Library*, Vol. 357, *Astrophysics and Space Science Library*, ed. W. Becker, 91
- Blondin, J. M., Wright, E. B., Borkowski, K. J., & Reynolds, S. P. 1998, *ApJ*, 500, 342
- Böhringer, H. & Werner, N. 2010, *A&A Rev.*, 18, 127
- Borkowski, K. J., Lyerly, W. J., & Reynolds, S. P. 2001, *ApJ*, 548, 820
- Busser, J.-U. 1998, PhD thesis, LMU, Germany
- Busser, J.-U., Egger, R., & Aschenbach, B. 1996, in *Roentgenstrahlung from the Universe*, ed. H. U. Zimmermann, J. Trümper, & H. Yorke, 239–240
- Clark, B. G. 1980, *A&A*, 89, 377
- Culhane, J. L. 1977, in *Astrophysics and Space Science Library*, Vol. 66, *Supernovae*, ed. D. N. Schramm, 29
- De Horta, A. Y., Collier, J. D., Filipović, M. D., et al. 2012, submitted to *MNRAS*
- de Luca, A. 2008, in *American Institute of Physics Conference Series*, Vol. 983, *40 Years of Pulsars: Millisecond Pulsars, Magnetars and More*, ed. C. Bassa, Z. Wang, A. Cumming, & V. M. Kaspi, 311–319
- Dickel, J. 1991, in *Supernovae*, ed. S. E. Woosley, 675
- Dickey, J. M. & Lockman, F. J. 1990, *ARA&A*, 28, 215
- Egger, R., Greiner, J., & Aschenbach, B. 1996, in *Roentgenstrahlung from the Universe*, ed. H. U. Zimmermann, J. Trümper, & H. Yorke, 247–248
- Folgheraiter, E. L., Watson, M. G., & Warwick, R. S. 1996, in *Roentgenstrahlung from the Universe*, ed. H. U. Zimmermann, J. Trümper, & H. Yorke, 253–254
- Gonzalez, M. & Safi-Harb, S. 2003, *ApJ*, 591, L143
- Gothelf, E. V. & Halpern, J. P. 2008, in *American Institute of Physics Conference Series*, Vol. 983, *40 Years of Pulsars: Millisecond Pulsars, Magnetars and More*, ed. C. Bassa, Z. Wang, A. Cumming, & V. M. Kaspi, 320–324
- Green, D. A. 2009, *Bulletin of the Astronomical Society of India*, 37, 45
- Guerrero, M. A., Chu, Y.-H., & Gruendl, R. A. 2000, *ApJS*, 129, 295
- Guerrero, M. A., Chu, Y.-H., & Gruendl, R. A. 2006, in *ESA Special Publication*, Vol. 604, *The X-ray Universe 2005*, ed. A. Wilson, 85
- Helfand, D. J., Velusamy, T., Becker, R. H., & Lockman, F. J. 1989, *ApJ*, 341, 151
- Hobbs, G., Lorimer, D. R., Lyne, A. G., & Kramer, M. 2005, *MNRAS*, 360, 974
- Jackson, M. S., Safi-Harb, S., Kothes, R., & Foster, T. 2008, *ApJ*, 674, 936
- Kalberla, P. M. W., Burton, W. B., Hartmann, D., et al. 2005, *A&A*, 440, 775
- Keane, E. F. & Kramer, M. 2008, *MNRAS*, 391, 2009
- Krautter, J., Zickgraf, F.-J., Appenzeller, I., et al. 1999, *A&A*, 350, 743
- Lucke, P. B. 1978, *A&A*, 64, 367
- Maccacaro, T., Gioia, I. M., Wolter, A., Zamorani, G., & Stocke, J. T. 1988, *ApJ*, 326, 680
- McKee, C. F. 1987, in *Spectroscopy of Astrophysical Plasmas*, ed. A. Dalgarno & D. Layzer, 226–254
- Mirabel, I. F. & Rodríguez, L. F. 1999, *ARA&A*, 37, 409
- Monet, D. G., Levine, S. E., Canzian, B., et al. 2003, *AJ*, 125, 984
- Osten, R. A., Hawley, S. L., Allred, J. C., Johns-Krull, C. M., & Roark, C. 2005, *ApJ*, 621, 398
- Pfeffermann, E. & Aschenbach, B. 1996, in *Roentgenstrahlung from the Universe*, ed. H. U. Zimmermann, J. Trümper, & H. Yorke, 267–268
- Phillips, J. P. 2006, *Rev. Mexicana Astron. Astrofis.*, 42, 229
- Predehl, P. & Schmitt, J. H. M. M. 1995, *A&A*, 293, 889
- Reich, W., Fuerst, E., & Arnal, E. M. 1992, *A&A*, 256, 214
- Robbins, W. J., Gaensler, B. M., Murphy, T., Reeves, S., & Green, A. J. 2011, *ArXiv e-prints*
- Safi-Harb, S., Harrus, I. M., Petre, R., et al. 2001, *ApJ*, 561, 308
- Sault, R. J., Teuben, P. J., & Wright, M. C. H. 1995, in *Astronomical Society of the Pacific Conference Series*, Vol. 77, *Astronomical Data Analysis Software and Systems IV*, ed. R. A. Shaw, H. E. Payne, & J. J. E. Hayes, 433
- Schaudel, D. 2003, PhD thesis, LMU, Germany
- Schaudel, D., Becker, W., Voges, W., et al. 2002, in *Astronomical Society of the Pacific Conference Series*, Vol. 271, *Neutron Stars in Supernova Remnants*, ed. P. O. Slane & B. M. Gaensler, 391
- Sedov, L. I. 1959, *Similarity and Dimensional Methods in Mechanics*, ed. Sedov, L. I.
- Seok, J. Y., Koo, B.-C., Onaka, T., et al. 2008, *PASJ*, 60, 453
- Slane, P., Chen, Y., Lazendic, J. S., & Hughes, J. P. 2002, *ApJ*, 580, 904
- Stupar, M., Parker, Q. A., Filipović, M. D., et al. 2007, *MNRAS*, 381, 377
- Sun, M., Wang, Z.-R., & Chen, Y. 1999, *ApJ*, 511, 274
- The Fermi-LAT Collaboration. 2011, *ArXiv e-prints*
- Tian, W. W., Li, Z., Leahy, D. A., et al. 2010, *ApJ*, 712, 790
- Whiteoak, J. B. Z. & Green, A. J. 1996, *A&AS*, 118, 329
- Wright, E. L., Eisenhardt, P. R. M., Mainzer, A. K., et al. 2010, *AJ*, 140, 1868
- Zombeck, M. 2007, *Handbook of Space Astronomy and Astrophysics: Third Edition*, ed. Zombeck, M. (Cambridge University Press)

<sup>4</sup> <http://heasarc.nasa.gov/Tools/w3pimms.html>